Acta Mech 229, 3375–3392 (2018)
https://doi.org/10.1007/s00707-018-2175-6

ORIGINAL PAPER

S. J. D. D'Alessio

Flow past a slippery cylinder: part 1—circular cylinder

Received: 9 January 2018 / Revised: 29 April 2018 / Published online: 21 May 2018

Abstract Part 1 of this two-part paper solves the two-dimensional problem of the unsteady flow of a viscous incompressible fluid past a circular cylinder subject to impermeability and Navier-slip conditions on the surface. The Navier-slip condition is characterized by the slip length, β. The flow is calculated using two methods. The first takes the form of a double series solution where an expansion is carried out in powers of the time, t, and in powers of the parameter $\lambda = \sqrt{8t/R}$ where R is the Reynolds number. This approximate analytical solution is valid for small times following the start of the motion and for large Reynolds numbers. The second method involves a spectral-finite difference procedure for numerically integrating the full Navier–Stokes equations expressed in terms of a stream function and vorticity. Our results demonstrate that for small times and moderately large R the two methods of solution are in excellent agreement. Results are presented for Reynolds numbers 500 and 1000, and comparisons with the no-slip condition are made. The key finding is that a reduction in the drag coefficient results from the Navier-slip condition when compared to the no-slip condition. This reduction increases as β increases. In addition, the slip condition also leads to suppression in flow separation.

1 Introduction

This research solves the problem of unsteady flow past a circular cylinder of radius a. For $t < 0$, both the cylinder and the surrounding fluid are at rest. Then suddenly at $t = 0$ the cylinder is impulsively set into motion and moves with uniform speed U_0 in the positive x direction. The problem is formulated in a reference frame that moves with the cylinder having the origin of the coordinate system coinciding with the center of the cylinder as shown in Fig. 1. The fluid is taken to be viscous and incompressible. The problem is solved on the premise that the governing equations are the Navier–Stokes equations and that the flow remains laminar and two-dimensional for all times and parameter values considered. On the cylinder surface, impermeability and Navier-slip conditions are applied while at large distances asymptotic conditions are imposed.

Flow past a circular cylinder has received enormous attention over the years due to its practical and fundamental importance. A comprehensive list of references detailing experimental, numerical and theoretical investigations for various flow configurations can be found in the texts by Zdravkovich [1,2]. It is fair to say that the vast majority of these investigations enforces no-slip conditions on the cylinder surface. Although the no-slip condition has become the default boundary condition applied at a solid–liquid interface, the validity of this condition was challenged at length during the nineteenth and early twentieth century. The notion of a slip condition was originally proposed by Navier [3]. Cases in which the no-slip condition is known to fail include the flows of rarified gases or flows within microfluidic/nanofluidic devices [4]. Here, the mean free path of the fluid approaches the characteristic length scale. For situations involving hydrophobic solids, a

S. J. D. D'Alessio (✉)
Department of Applied Mathematics, University of Waterloo, Waterloo, ON N2L 3G1, Canada
E-mail: sdalessio@uwaterloo.ca

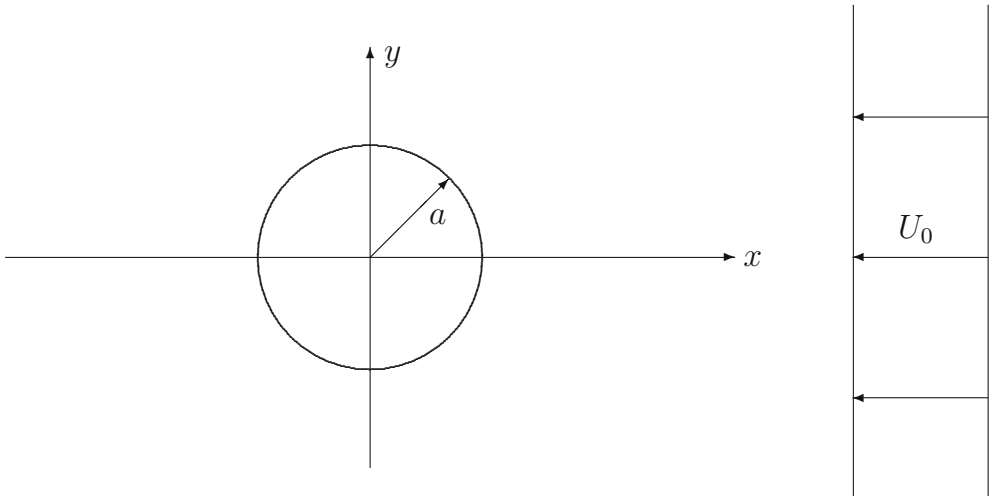

Fig. 1 Flow setup

general Navier-slip condition yields results that are in better agreement with experimental observations than the traditional no-slip condition [5]. Beavers and Joseph [6] proposed a semiempirical slip condition for a liquid-porous medium interface which was later extended by Saffman [7].

The surface roughness scale distinguishes hydrophobic surfaces from superhydrophobic surfaces. Hydrophobic surfaces can be characterized as having micron-sized protrusions, while superhydrophobic surfaces typically have nanometer-sized ridges or posts. The importance of superhydrophobic surfaces lies in the observation that these surfaces have been shown to produce a significant reduction in drag for both laminar and turbulent flows. Although the boundary condition experienced by a fluid over a superhydrophobic surface is no-slip, the air–fluid interfaces existing between the surface features are essentially shear free and hence responsible for reducing drag. The engineering of superhydrophobic surfaces has impacted various technologies ranging from microfluidic/nanofluidic devices to marine vessels.

Relatively few studies have been devoted to slip flow past a cylinder. Three related previous studies in particular are worth noting. You and Moin [8] studied the impact that hydrophobic surfaces have on the drag and lift coefficients. They did this by comparing cylinders having a no-slip surface, a slip surface and a cylinder having alternating bands of slip and no-slip conditions for Reynolds numbers of 300 and 3900 using direct numerical simulations and large-eddy simulations. They found that for large Reynolds numbers hydrophobic surfaces can lead to a reduction in drag and lift. Seo and Song [9], on the other hand, investigated the influence of partial-slip conditions on the laminar flow past a circular cylinder using the shallow-water equations for Reynolds numbers of 20, 40, 80, and 100. They found a reduction in drag as the slip length increased. Lastly, Li et al. [10] looked at various slip configurations using analytical and numerical techniques for small-to-moderately-large Reynolds numbers. For the Reynolds number range of 100–500, they discovered that flank slip conditions produced the largest reduction in drag.

The underlying assumption made in this study is that the flow remains two-dimensional and laminar. One can argue that for the Reynolds number regime considered three-dimensional effects and turbulence may significantly alter the flow. In fact, experimental work conducted by Williamson [11] for the case of a circular cylinder suggests that a three-dimensional transition occurs for Reynolds numbers $R > 178$. We also note, however, that the three-dimensionality can be suppressed or delayed experimentally in several ways. For example, the work of Blackburn and Henderson [12] has shown that cylinder vibrations tend to suppress the three-dimensionality and produce flows that are more two-dimensional than their fixed cylinder counterparts. Also, the results to be presented in this investigation suggest that the flow past a slippery cylinder becomes more streamlined and that flow separation is suppressed. Based on this one would be inclined to infer that this should also delay the onset of three-dimensionality and hence support the two-dimensional simplification. Although physically the wake may be three-dimensional and turbulent, we believe that it can be represented reasonably well by a laminar two-dimensional model in the near-wake region which is the focus of this study.

The main contributions of the present research are twofold. First, an analytical solution for the early development of the flow is derived. This approximate solution is valid for small times, t, and moderate-to-high Reynolds numbers, R. This represents an important contribution to this problem because currently only low-to-

moderate Reynolds number approximate solutions exist in the literature [10]. Second, an efficient numerical technique for solving the Navier–Stokes equations is proposed. This scheme is significantly different than those used in previous numerical studies. An advantage offered by the analytical solution is that it provides a means of validating the numerical solution for small times, and the reconciling of our numerical and analytical solutions will be demonstrated. In addition, a detailed comparison between the slip and no-slip cases is carried out.

This two-part paper is organized as follows: We begin in Sect. 2 by presenting the governing equations along with their corresponding initial and boundary conditions using a coordinate system well suited for the geometry. We also introduce boundary-layer coordinates as a means of better representing the initial flow structure. Then, in Sect. 3, we construct an analytical solution to elicit information regarding the early flow development. This is achieved by performing an expansion in powers of the parameter $\lambda = \sqrt{8t/R}$, followed by an expansion in terms of t. This procedure yields a series solution for the flow variables which is valid for small times and large values of R. Following this, a numerical method for solving the governing equations is outlined in Sect. 4. Comparisons and discussion between numerical and analytical results, along with streamline plots and comparisons using the no-slip condition, are presented in Sect. 5. Lastly, the work is summarized in Sect. 6. Part 2 of this paper represents an extension to slip flow past an inclined elliptic cylinder.

2 Governing equations

Assuming the flow remains two-dimensional for all time, a good choice of flow variables to describe the motion is the scalar stream function, ψ, and vorticity, ζ. In terms of modified polar coordinates (ξ, θ) where $\xi = \ln r$, the governing Navier–Stokes equations in dimensionless form are given by

$$\frac{\partial^2 \psi}{\partial \xi^2} + \frac{\partial^2 \psi}{\partial \theta^2} = \mathrm{e}^{2\xi}\zeta, \tag{1}$$

$$\mathrm{e}^{2\xi}\frac{\partial \zeta}{\partial t} = \frac{\partial \psi}{\partial \theta}\frac{\partial \zeta}{\partial \xi} - \frac{\partial \psi}{\partial \xi}\frac{\partial \zeta}{\partial \theta} + \frac{2}{R}\left(\frac{\partial^2 \zeta}{\partial \xi^2} + \frac{\partial^2 \zeta}{\partial \theta^2}\right). \tag{2}$$

We seek a solution in the domain $\xi \geq 0$ and $0 \leq \theta \leq 2\pi$. The dimensionless radial and transverse velocity components (u, v) can be obtained using

$$u = -\mathrm{e}^{-\xi}\frac{\partial \psi}{\partial \theta}, \quad v = \mathrm{e}^{-\xi}\frac{\partial \psi}{\partial \xi}. \tag{3}$$

The dimensionless functions ψ and ζ are related to their dimensional counterparts ψ^* and ζ^* by $\psi^* = aU_0\psi$ and $\zeta^* = U_0\zeta/a$, while the dimensionless time, t, and radial coordinate, r, are related to the dimensional time t^* by $t^* = at/U_0$ and dimensional coordinate r^* by $r^* = ar$. Here, R denotes the Reynolds number defined by $R = 2aU_0/\nu$ where ν is the kinematic viscosity.

The surface boundary conditions include the impermeability and Navier-slip conditions given by

$$u = 0, \quad v = \beta\frac{\partial v}{\partial \xi} \text{ at } \xi = 0,$$

respectively. The Navier-slip condition adopted in this study corresponds to the Beavers and Joseph [6] condition. Here, β denotes the dimensionless slip length and is related to the dimensional slip length β^* by $\beta = \beta^*/a$. Physically, the dimensional slip length refers to the distance required for the slip velocity at the surface to decrease to zero and hence become no-slip. Thus, as expected, $\beta = 0$ recovers the no-slip condition. For a porous material, $\beta^* = \sqrt{\Pi}/\Lambda$ where Π is the permeability and Λ is the Beavers–Joseph constant which takes on values between 0.1 and 0.4 [6]; for common materials, $\sqrt{\Pi}$ can be as large as 10^{-2} mm [13]. In terms of ψ and ζ, these conditions become

$$\psi = 0, \quad \frac{\partial \psi}{\partial \xi} = \frac{\beta}{(1+\beta)}\zeta \text{ at } \xi = 0. \tag{4}$$

In addition, we have the periodicity conditions

$$\psi(\xi, \theta, t) = \psi(\xi, \theta + 2\pi, t), \quad \zeta(\xi, \theta, t) = \zeta(\xi, \theta + 2\pi, t), \tag{5}$$

and the far-field conditions

$$\psi \to \mathrm{e}^{\xi} \sin\theta \ , \ \ \zeta \to 0 \text{ as } \xi \to \infty. \tag{6}$$

Condition (6) results from the oncoming uniform flow. Inspecting the boundary conditions (4), we notice a coupling between the surface vorticity and the normal derivative of the stream function which may be difficult to implement numerically. An alternate method to deal with this involves the use of integral conditions, which we next introduce.

Dennis and Quartapelle [14] have shown that the vorticity satisfies integral constraints which can be derived from Green's second identity using the known surface and far-field boundary conditions. Recall that Green's second identity states that any twice differentiable functions g and h in the region D satisfy

$$\int\int_D (g\nabla^2 h - h\nabla^2 g)\mathrm{d}x\mathrm{d}y = \oint_C \left(g\frac{\partial h}{\partial n} - h\frac{\partial g}{\partial n}\right)\mathrm{d}S.$$

Here, $\partial h/\partial n$, $\partial g/\partial n$ refer to normal derivatives, and C is the closed curve corresponding to the boundary of D. Choosing $g = \psi$ and h to be harmonic functions given by $\mathrm{e}^{-n\xi}\sin(n\theta)$ and $\mathrm{e}^{-n\xi}\cos(n\theta)$, it is a straightforward exercise to show that the vorticity satisfies integral constraints given by

$$\int_0^\infty \int_0^{2\pi} \mathrm{e}^{(2-n)\xi}\zeta(\xi,\theta,t)\sin(n\theta)\mathrm{d}\theta d\xi = 2\pi\delta_{1,n} - \frac{\beta}{(1+\beta)}\int_0^{2\pi}\zeta(0,\theta,t)\sin(n\theta)\mathrm{d}\theta, \tag{7}$$

for $n = 1, 2, \ldots$, and

$$\int_0^\infty \int_0^{2\pi} \mathrm{e}^{(2-n)\xi}\zeta(\xi,\theta,t)\cos(n\theta)d\theta d\xi = -\frac{\beta}{(1+\beta)}\int_0^{2\pi}\zeta(0,\theta,t)\cos(n\theta)\mathrm{d}\theta, \tag{8}$$

for $n = 0, 1, 2, \ldots$, where $\delta_{i,n}$ is the Kronecker delta, defined by

$$\delta_{i,n} = \begin{cases} 1 & \text{if } n = i \\ 0 & \text{if } \ n \neq i \end{cases}.$$

Basically, Green's second identity enables us to convert the known boundary conditions on the surface and at large distances into conditions that are valid throughout the entire domain. The issue now becomes how to use these integral conditions to determine the, as of yet, unknown surface vorticity. This will be fully explained in the subsequent sections.

Because of the impulsive start imposed on the flow, a thin boundary layer of thickness $\sqrt{8t/R}$ surrounds the cylinder. To better accommodate this singular behavior, we stretch the coordinate ξ and flow variables according to

$$\xi = \lambda z, \ \ \psi = \lambda\Psi, \ \ \zeta = \omega/\lambda \ \ \text{where} \ \ \lambda = \sqrt{\frac{8t}{R}}\ . \tag{9}$$

In terms of the boundary-layer coordinates (z, θ), Eqs. (1)–(2) transform to

$$\frac{\partial^2\Psi}{\partial z^2} + \lambda^2\frac{\partial^2\Psi}{\partial\theta^2} = \mathrm{e}^{2\lambda z}\omega\ , \tag{10}$$

$$\frac{\partial^2\omega}{\partial z^2} + 2\mathrm{e}^{2\lambda z}\left(z\frac{\partial\omega}{\partial z} + \omega\right) = 4t\mathrm{e}^{2\lambda z}\frac{\partial\omega}{\partial t} - \lambda^2\frac{\partial^2\omega}{\partial\theta^2} - 4t\left(\frac{\partial\Psi}{\partial\theta}\frac{\partial\omega}{\partial z} - \frac{\partial\Psi}{\partial z}\frac{\partial\omega}{\partial\theta}\right), \tag{11}$$

and will be used to dictate the early stages of the flow. We emphasize that although boundary-layer coordinates are utilized, the full Navier–Stokes equations are to be solved and not the simplified boundary-layer equations. This transformation along with the integral conditions has been successfully used in previous studies, such as Badr and Dennis [15] and Collins and Dennis [16] for uniform flow past a cylinder, and Rohlf and D'Alessio [17] for shear flow past a cylinder.

In the next section, we present a procedure by which we can build up an approximate solution for small times and large Reynolds numbers, and in the process we will be able to determine the initial solution which can be used as an initial condition.

3 Analytical solution procedure

If R is large and t is small, then λ is also small, and it is possible to expand the flow variables in a double series in terms of λ and t. First, we expand Ψ and ω in a series of the form

$$\begin{aligned}\Psi &= \Psi_0 + \lambda\Psi_1 + \lambda^2\Psi_2 + \cdots,\\ \omega &= \omega_0 + \lambda\omega_1 + \lambda^2\omega_2 + \cdots.\end{aligned} \tag{12}$$

Then each $\Psi_n, \omega_n, n = 0, 1, 2, \ldots$, can be further expanded in a series of the form

$$\begin{aligned}\Psi_n(z,\theta,t) &= \Psi_{n0}(z,\theta) + t\Psi_{n1}(z,\theta) + \cdots,\\ \omega_n(z,\theta,t) &= \omega_{n0}(z,\theta) + t\omega_{n1}(z,\theta) + \cdots.\end{aligned} \tag{13}$$

We note that when performing a double expansion the internal orders of magnitudes between the expansion parameters should be taken into account. In our case, λ and t will be equal when $t = 8/R$, and thus, for a fixed value of R the procedure is expected to be valid for times that are of order $1/R$, provided that R is sufficiently large. Fortunately, asymptotic expansions are known to have the redeeming feature that they can provide good results outside the domain of validity. This will be discussed in more detail when we make comparisons with numerical solutions.

Substituting series (12)–(13) into Eqs. (10)–(11) and using the expansion

$$e^{2\lambda z} = 1 + 2\lambda z + 2\lambda^2 z^2 + \cdots,$$

produces a hierarchy of problems at various orders. For example, the first terms in the series, Ψ_0 and ω_0, correspond to the boundary-layer solution since they emerge in the limit as $R \to \infty$ and are valid for all $t \geq 0$. The boundary-layer equations are given by

$$\frac{\partial^2\Psi_0}{\partial z^2} = \omega_0, \tag{14}$$

$$\frac{\partial^2\omega_0}{\partial z^2} + 2z\frac{\partial\omega_0}{\partial z} + 2\omega_0 = 4t\frac{\partial\omega_0}{\partial t} - 4t\left(\frac{\partial\Psi_0}{\partial\theta}\frac{\partial\omega_0}{\partial z} - \frac{\partial\Psi_0}{\partial z}\frac{\partial\omega_0}{\partial\theta}\right). \tag{15}$$

The above equations expose the need for the double series; Eqs. (14)–(15) are still much too complicated to solve analytically, and so an expansion in t is also necessary to make analytical progress.

The initial solution at $t = 0$ corresponds to the terms Ψ_{00} and ω_{00} and can be obtained by setting $t = 0$ in Eqs. (14)–(15). The initial solution then satisfies

$$\frac{\partial^2\Psi_{00}}{\partial z^2} = \omega_{00}, \tag{16}$$

$$\frac{\partial^2\omega_{00}}{\partial z^2} + 2z\frac{\partial\omega_{00}}{\partial z} + 2\omega_{00} = 0. \tag{17}$$

It can easily be shown that the solution to (17) satisfying all the conditions is $\omega_{00} = 0$. Using this and integrating (16) twice and imposing the impermeability condition yields $\Psi_{00} = A(\theta)z$. The function $A(\theta)$ can be determined by applying the Navier-slip condition which when expanded yields

$$\frac{\partial\Psi_{00}}{\partial z} = \frac{\beta}{(1+\beta)}\omega_{10} \quad \text{at } z = 0.$$

Thus, in order to determine Ψ_{00} we first need to solve for ω_{10}. Before proceeding to find ω_{10}, we first point out that it is a straightforward exercise to show that $\omega_{0n} = 0$ for $n = 0, 1, 2, \ldots$.

The term ω_{10} satisfies the equation

$$\frac{\partial^2\omega_{10}}{\partial z^2} + 2z\frac{\partial\omega_{10}}{\partial z} = 0. \tag{18}$$

The solution satisfying the far-field condition $\omega_{10} \to 0$ as $z \to \infty$ is given by

$$\omega_{10}(z,\theta) = B(\theta)\operatorname{erfc}(z),$$

where $\mathrm{erfc}(z) = 1 - \mathrm{erf}(z)$ is the complementary error function while

$$\mathrm{erf}(z) = \frac{2}{\sqrt{\pi}} \int_0^z \mathrm{e}^{-u^2} \mathrm{d}u$$

denotes the error function. The function $B(\theta)$ can be determined by applying the integral conditions (7)–(8) which when expanded and expressed in terms of boundary-layer coordinates yield

$$\int_0^{2\pi} \omega_{10}(0,\theta) \sin(n\theta) \mathrm{d}\theta = \frac{2\pi(1+\beta)}{\beta} \delta_{1,n}, \quad \int_0^{2\pi} \omega_{10}(0,\theta) \cos(n\theta) \mathrm{d}\theta = 0.$$

It immediately follows that

$$B(\theta) = \frac{2(1+\beta)}{\beta} \sin\theta \quad \text{and hence} \quad A(\theta) = \frac{\beta}{(1+\beta)} B(\theta) = 2\sin\theta.$$

Thus, the leading-order nonzero terms in the solution become

$$\Psi_{00}(z,\theta) = 2z\sin\theta \ , \ \omega_{10}(z,\theta) = \frac{2(1+\beta)}{\beta} \mathrm{erfc}(z) \sin\theta.$$

Further, it was also shown that $\omega_{11} = \Psi_{01} = 0$. Examining the initial solution for the stream function, we observe that Ψ_{00} does not comply with the far-field condition (6). We have chosen to satisfy the surface conditions (4) at the expense of the far-field condition. It is much more important to satisfy the conditions on the surface because we are primarily interested in the evolving boundary-layer structure where vorticity is generated. Note, however, that ω_{10} is constructed in such a way that the far-field condition is automatically satisfied. This is a consequence of applying the integral conditions which incorporate the far-field conditions.

We now continue the procedure of determining the next terms, Ψ_{10} and ω_{20}, in the series given by (12). As we will see the procedure gets more and more complicated as more terms are sought. We begin by solving for ω_{20} which satisfies

$$\frac{\partial^2 \omega_{20}}{\partial z^2} + 2z \frac{\partial \omega_{20}}{\partial z} - 2\omega_{20} = -4z^2 \frac{\partial \omega_{10}}{\partial z}, \tag{19}$$

and must obey the far-field condition $\omega_{20} \to 0$ as $z \to \infty$ along with the integral conditions

$$\int_0^{\infty} \int_0^{2\pi} \omega_{10}(z,\theta) \sin(n\theta) \mathrm{d}\theta \mathrm{d}z = -\frac{\beta}{(1+\beta)} \int_0^{2\pi} \omega_{20}(0,\theta) \sin(n\theta) \mathrm{d}\theta,$$
$$\int_0^{\infty} \int_0^{2\pi} \omega_{10}(z,\theta) \cos(n\theta) \mathrm{d}\theta \mathrm{d}z = -\frac{\beta}{(1+\beta)} \int_0^{2\pi} \omega_{20}(0,\theta) \cos(n\theta) \mathrm{d}\theta.$$

Using the known solution for $\omega_{10}(z,\theta)$ and after some algebra, we obtain

$$\omega_{20}(z,\theta) = \frac{2(1+\beta)^2}{\sqrt{\pi}\beta^2} \left(\sqrt{\pi} z \mathrm{erfc}(z) - \mathrm{e}^{-z^2} \right) \sin\theta - \frac{(1+\beta)}{\beta} \left(z\mathrm{erfc}(z) + \frac{2}{\sqrt{\pi}} z^2 \mathrm{e}^{-z^2} \right) \sin\theta.$$

Next we solve for Ψ_{10} which satisfies

$$\frac{\partial^2 \Psi_{10}}{\partial z^2} = \omega_{10}, \tag{20}$$

subject to

$$\Psi_{10} = 0 \ , \ \frac{\partial \Psi_{10}}{\partial z} = \frac{\beta}{(1+\beta)} \omega_{20} \ \text{ at } \ z = 0.$$

Again, using the known solutions for $\omega_{10}(z,\theta)$ and $\omega_{20}(z,\theta)$ we obtain

$$\Psi_{10}(z,\theta) = \frac{2(1+\beta)}{\beta} \left(\frac{z^2}{2} \mathrm{erfc}(z) - \frac{1}{4} \mathrm{erf}(z) - \frac{z}{2\sqrt{\pi}} \mathrm{e}^{-z^2} \right) \sin\theta.$$

The approximate solution

$$\Psi \sim \Psi_{00} + \lambda\ \Psi_{10}\ ,\ \ \omega \sim \lambda\ \omega_{10} + \lambda^2\ \omega_{20}$$

determined here provides sufficient information to validate the numerical scheme, outlined in the following section, for small times. As a physical check of the analytical solution found, we compare the solution with the inviscid solution which is easily found to be

$$\psi(\xi, \theta) = 2 \sinh \xi \sin \theta,\ \ \zeta(\xi, \theta) = 0.$$

Then,

$$v = \mathrm{e}^{-\xi} \frac{\partial \psi}{\partial \xi} = 2 \sin \theta \ \ \text{at}\ \ \xi = 0.$$

In the large R limit, the transverse velocity according to our expansion becomes

$$v = \frac{\partial \Psi_{00}}{\partial z}.$$

Evaluating this in the limit as $z \to \infty$, we obtain

$$v \to 2 \sin \theta,$$

which is in full agreement with the surface transverse velocity predicted by inviscid flow. Lastly, as a final comment we note that although $\beta \geq 0$ it is worth entertaining the consequences of a negative value of β even though it is not physical or realistic. For example, when $\beta = -1$ the surface vorticity is zero, and the analytical solution appears to reduce to the inviscid solution.

4 Numerical solution procedure

We now present a numerical method used to solve Eqs. (10)–(11). The numerical technique implemented here is a spectral-finite difference scheme which is successful in capturing the early development of the flow. Actually, the scheme employed represents a modified version of those utilized by Badr and Dennis [15] and Rohlf and D'Alessio [17].

We begin by expanding the flow variables in an infinite Fourier series having the form

$$\begin{aligned} \Psi(z, \theta, t) &= \frac{F_0(z, t)}{2} + \sum_{n=1}^{\infty} [F_n(z, t) \cos(n\theta) + f_n(z, t) \sin(n\theta)]\ , \\ \omega(z, \theta, t) &= \frac{G_0(z, t)}{2} + \sum_{n=1}^{\infty} [G_n(z, t) \cos(n\theta) + g_n(z, t) \sin(n\theta)]\ . \end{aligned} \tag{21}$$

When these are substituted into Eqs. (10)–(11), we obtain the following equations for the Fourier coefficients:

$$\frac{\partial^2 F_0}{\partial z^2} = \mathrm{e}^{2\lambda z} G_0(z, t); \tag{22}$$

$$\frac{\partial^2 F_n}{\partial z^2} - n^2 \lambda^2 F_n = \mathrm{e}^{2\lambda z} G_n(z, t);\ \ n = 1, 2, \ldots, \tag{23}$$

$$\frac{\partial^2 f_n}{\partial z^2} - n^2 \lambda^2 f_n = \mathrm{e}^{2\lambda z} g_n(z, t);\ \ n = 1, 2, \ldots, \tag{24}$$

$$\mathrm{e}^{-2\lambda z} \frac{\partial^2 G_0}{\partial z^2} + 2z \frac{\partial G_0}{\partial z} + 2G_0 = 4t \frac{\partial G_0}{\partial t} - 4t \mathrm{e}^{-2\lambda z} S_0, \tag{25}$$

$$\mathrm{e}^{-2\lambda z}\frac{\partial^2 G_n}{\partial z^2}+\left(2z+4nt\mathrm{e}^{-2\lambda z}f_{2n}\right)\frac{\partial G_n}{\partial z}+\left(2-n^2\lambda^2\mathrm{e}^{-2\lambda z}+2nt\mathrm{e}^{-2\lambda z}\frac{\partial f_{2n}}{\partial z}\right)G_n=4t\frac{\partial G_n}{\partial t}$$
$$-2nt\mathrm{e}^{-2\lambda z}\left(f_n\frac{\partial G_0}{\partial z}-g_n\frac{\partial F_0}{\partial z}-g_n\frac{\partial F_{2n}}{\partial z}-2F_{2n}\frac{\partial g_n}{\partial z}\right)-2t\mathrm{e}^{-2\lambda z}S_n\ ;\ n=1,2,\ldots, \tag{26}$$

$$\mathrm{e}^{-2\lambda z}\frac{\partial^2 g_n}{\partial z^2}+\left(2z-4nt\mathrm{e}^{-2\lambda z}f_{2n}\right)\frac{\partial g_n}{\partial z}+\left(2-n^2\lambda^2\mathrm{e}^{-2\lambda z}-2nt\mathrm{e}^{-2\lambda z}\frac{\partial f_{2n}}{\partial z}\right)g_n=4t\frac{\partial g_n}{\partial t}$$
$$+2nt\mathrm{e}^{-2\lambda z}\left(F_n\frac{\partial G_0}{\partial z}-G_n\frac{\partial F_0}{\partial z}+G_n\frac{\partial F_{2n}}{\partial z}+2F_{2n}\frac{\partial G_n}{\partial z}\right)-2t\mathrm{e}^{-2\lambda z}T_n\ ;\ n=1,2,\ldots \tag{27}$$

where

$$S_0=\sum_{n=1}^{\infty}\frac{\partial}{\partial z}[n(f_nG_n-F_ng_n)],$$
$$S_n=\sum_{\substack{m=1\\m\neq n}}^{\infty}\left(\frac{\partial G_m}{\partial z}[(m+n)f_{m+n}+|m-n|f_{|m-n|}]+mG_m\left[\frac{\partial f_{m+n}}{\partial z}+\mathrm{sgn}(m-n)\frac{\partial f_{|m-n|}}{\partial z}\right]\right.$$
$$\left.-mg_m\left[\frac{\partial F_{m+n}}{\partial z}+\frac{\partial F_{|m-n|}}{\partial z}\right]-\frac{\partial g_m}{\partial z}[(m+n)F_{m+n}+(m-n)F_{|m-n|}]\right),$$
$$T_n=\sum_{\substack{m=1\\m\neq n}}^{\infty}\left(\frac{\partial g_m}{\partial z}[|m-n|f_{|m-n|}-(m+n)f_{m+n}]-mG_m\left[\frac{\partial F_{m+n}}{\partial z}-\frac{\partial F_{|m-n|}}{\partial z}\right]\right.$$
$$\left.-mg_m\left[\frac{\partial f_{m+n}}{\partial z}-\mathrm{sgn}(m-n)\frac{\partial f_{|m-n|}}{\partial z}\right]-\frac{\partial G_m}{\partial z}[(m+n)F_{m+n}-(m-n)F_{|m-n|}]\right).$$

Here, $\mathrm{sgn}(m-n)$ denotes the sign of $m-n$ with $\mathrm{sgn}(0)=0$. In theory, the system of Eqs. (22)–(27) comprises an infinite set; in practice, however, we truncate series (21) by setting all terms having subscripts $n>N$ to zero. Systems (22)–(27) then consist of $4N+2$ equations.

We now outline the solution procedure for the Fourier coefficients $F_0, G_0, F_n, G_n, f_n, g_n$ for $n=1,2,\ldots,N$. We need to solve Eqs. (25)–(27) subject to the far-field conditions

$$G_0\to 0\ ,\ G_n, g_n\to 0\ \text{ as }\ z\to\infty\ \text{ for }\ n=1,2,\ldots,N,$$

and the integral conditions (7)–(8) which now become

$$\int_0^{\infty}\mathrm{e}^{(2-n)\lambda z}G_n(z,t)\mathrm{d}z=-\frac{\beta}{\lambda(1+\beta)}G_n(0,t)\ \text{ for }\ n=0,1,2,\ldots,N\ ,$$
$$\int_0^{\infty}\mathrm{e}^{(2-n)\lambda z}g_n(z,t)dz=2\delta_{1,n}-\frac{\beta}{\lambda(1+\beta)}g_n(0,t)\ \text{ for }\ n=1,2,\ldots,N. \tag{28}$$

We illustrate the method using Eq. (25) with the understanding that (26)–(27) are solved in a similar manner. Equation (25) may be rewritten in the form

$$4t\frac{\partial G_0}{\partial t}=Q(z,t) \tag{29}$$

where

$$Q(z,t)=\mathrm{e}^{-2\lambda z}\frac{\partial^2 G_0}{\partial z^2}+2z\frac{\partial \hat{G}_0}{\partial z}+2G_0+4t\mathrm{e}^{-2\lambda z}S_0. \tag{30}$$

Assuming the solution at time t is known, we can advance the solution to time $t+\Delta t$ by integrating Eq. (29). Integration by parts yields

$$4\tau G_0\big|_t^{t+\Delta t}-4\int_t^{t+\Delta t}G_0d\tau=\int_t^{t+\Delta t}Q\mathrm{d}\tau$$

where Δt is the time increment. We now approximate the integrals using

$$\int_t^{t+\Delta t} \chi\, d\tau \approx \Delta t[\varpi\,\chi(z, t+\Delta t) + (1-\varpi)\chi(z,t)]$$

where ϖ is a weight factor and χ is a generic function. In general, $0 \le \varpi \le 1$ and we treat ϖ as a computational parameter still to be specified. When $\varpi = 1/2$, we obtain the well-known Crank–Nicolson scheme, while $\varpi = 1$ yields the fully implicit scheme. The case $\varpi = 0$ corresponds to an explicit scheme which will not be considered. With this approximation in place, Eq. (29) brings us to the expression

$$4[t + (1-\varpi)\Delta t](G_0(z, t+\Delta t) - G_0(z,t)) = \Delta t[\varpi\, Q(z, t+\Delta t) + (1-\varpi)Q(z,t)]. \tag{31}$$

If we now substitute $Q(z, t+\Delta t)$ given by (30) into (31) and replace all derivatives of G_0 with respect to z by central differences at the point z, then (31) becomes

$$\begin{aligned} &C_1(z, t+\Delta t)G_0(z-\Delta z, t+\Delta t) + C_2(z, t+\Delta t)G_0(z, t+\Delta t) \\ &\quad + C_3(z, t+\Delta t)G_0(z+\Delta z, t+\Delta t) = D(z, t+\Delta t) + E(z,t) \end{aligned} \tag{32}$$

where Δz is the uniform grid spacing in the z direction and the functions C_1, C_2, C_3, D, E can be easily derived and do not involve G_0. The function E is known from the previous time step, while the functions C_1, C_2, C_3, D are computed using the most recent available information as an initial guess. Thus, when represented in matrix form Eq. (32) becomes a tri-diagonal system for the unknown values of G_0 at the grid points $z = 0, \Delta z, 2\Delta z, \ldots$. If the region $0 \le z \le z_\infty$, with z_∞ denoting the outer boundary approximating infinity, is divided into L equally spaced intervals of Δz, then an $(L-1)\times(L-1)$ tri-diagonal matrix results.

At each time step, we need to solve this system subject to the far-field condition $G_0(z_\infty, t+\Delta t) = 0$ and the integral conditions given by (28). To enforce the integral conditions, we proceed as follows: First, we obtain the homogeneous solution, G_0^h, by setting the right-hand side in (32) to zero, with G_0^h satisfying $G_0^h(0, t+\Delta t) = 1$ and $G_0^h(z_\infty, t+\Delta t) = 0$. Then, we find the particular solution, G_0^p, to (32) again satisfying $G_0^p(0, t+\Delta t) = 1$ and $G_0^p(z_\infty, t+\Delta t) = 0$. We form the complete solution as

$$G_0(z, t+\Delta t) = \gamma G_0^h(z, t+\Delta t) + G_0^p(z, t+\Delta t).$$

Finally, the constant γ is chosen so that (28) is satisfied. This yields

$$\gamma = -\frac{\left(\frac{\beta}{\lambda(1+\beta)} + \int_0^{z_\infty} \mathrm{e}^{2\lambda z} G_0^p\, dz\right)}{\left(\frac{\beta}{\lambda(1+\beta)} + \int_0^{z_\infty} \mathrm{e}^{2\lambda z} G_0^h \mathrm{d}z\right)}.$$

The integrals appearing in the expression for γ are computed by Simpson's rule, while an efficient routine is implemented to solve the tri-diagonal systems for G_0^h and G_0^p. With our approximate solution to $G_0(z, t+\Delta t)$ now found, we then repeat this procedure for obtaining approximate solutions to $G_n(z, t+\Delta t)$, $g_n(z, t+\Delta t)$ for $n = 1, 2, \ldots, N$.

The system given by (22)–(24) is effectively a linear system of ordinary differential equations, and there are numerous methods available to solve such a system. The method used here to solve (22)–(24) for the stream function is identical to that outlined in Dennis and Chang [18] and will be briefly described. First, the right-hand sides of these equations are obtained using the computed solutions G_0, G_n, g_n for $n = 1, 2, \ldots, N$. Then, each of these equations is factored into a pair of first-order equations, one of which is integrated in the direction of increasing z, while the other in the direction of decreasing z. These first-order equations are then integrated using stable marching algorithms satisfying the Navier-slip and impermeability conditions

$$F_0 = F_n = f_n = 0, \quad \frac{\partial F_0}{\partial z} = \frac{\beta}{\lambda(1+\beta)} G_0, \quad \frac{\partial F_n}{\partial z} = \frac{\beta}{\lambda(1+\beta)} G_n, \quad \frac{\partial f_n}{\partial z} = \frac{\beta}{\lambda(1+\beta)} g_n,$$

at $z = 0$ for $n = 1, 2, \ldots, N$ and the far-field conditions

$$F_0 \to 0, \quad F_n \to 0, \quad f_n \to \frac{1}{\lambda}\mathrm{e}^{\lambda z}\delta_{1,n} \quad \text{as} \quad z \to \infty \quad \text{for} \quad n = 1, 2, \ldots, N\ .$$

Before outlining the marching schemes utilized, we first recognize that at a given time t the equations for f_n, F_n can be viewed as linear differential equations of the type

$$\frac{d^2\mathcal{F}}{dz^2} - \kappa^2\mathcal{F} = c(z) \tag{33}$$

where $\mathcal{F} = \mathcal{F}(z)$ is one of f_n, F_n, $\kappa = n\lambda$, and $c(z)$ depends on the vorticity coefficients g_n, G_n. We assume that $\mathcal{F}$ and c are spatially discretized according to $\mathcal{F}_j = \mathcal{F}(j\Delta z)$ and $c_j = c(j\Delta z)$. The important point to note here is that the particular marching algorithm to be used is dependent on the parameter $\kappa = n\lambda$. It is shown in Dennis and Chang [18] that most step-by-step procedures become increasingly unstable as κ becomes large. Hence, two sets of step-by-step methods are utilized: one for the case $\kappa < 0.5$ while another for $\kappa \geq 0.5$. The details for both cases will be outlined below.

For $\kappa < 0.5$, we make use of the marching scheme

$$\mathcal{F}_{j+1} = \frac{24 + 10\kappa^2\Delta z^2}{12 - \kappa^2\Delta z^2}\mathcal{F}_j - \mathcal{F}_{j-1} + \frac{\Delta z^2}{12 - \kappa^2\Delta z^2}\left(c_{j+1} + 10c_j + c_{j-1}\right), \tag{34}$$

which is accurate to $O(\Delta z^6)$. The marching procedure is initiated with the lower-order scheme

$$\mathcal{F}_1 = \frac{\Delta z^2}{6}(2c_0 + c_1) + \frac{\mathrm{d}\mathcal{F}_0}{\mathrm{d}z}\left(\Delta z + \frac{\kappa^2\Delta z^3}{6}\right), \tag{35}$$

which makes use of the boundary conditions $\mathcal{F}_0 = 0$.

For $\kappa \geq 0.5$, we use the idea of Dennis and Chang [18] that equation (33) can be factored as

$$\left(\frac{\mathrm{d}}{\mathrm{d}z} - \kappa\right)\left(\frac{\mathrm{d}}{\mathrm{d}z} + \kappa\right)\mathcal{F} = c(z). \tag{36}$$

We can now make the change of variables

$$p = \frac{\mathrm{d}\mathcal{F}}{\mathrm{d}z} + \kappa\mathcal{F}, \tag{37}$$

$$q = \frac{\mathrm{d}\mathcal{F}}{\mathrm{d}z} - \kappa\mathcal{F}. \tag{38}$$

This allows Eq. (36) to be written as the non-coupled system of first-order differential equations

$$\frac{\mathrm{d}p}{\mathrm{d}z} - \kappa p = c(z), \tag{39}$$

$$\frac{\mathrm{d}q}{\mathrm{d}z} + \kappa q = c(z). \tag{40}$$

Once p and q have been solved, $\mathcal{F}$ and $\frac{d\mathcal{F}}{dz}$ can be obtained by the relations

$$\mathcal{F} = \frac{p - q}{2\kappa}, \tag{41}$$

$$\frac{\mathrm{d}\mathcal{F}}{\mathrm{d}z} = \frac{p + q}{2}. \tag{42}$$

Equation (39) is marched forwards from $z = 0$ to $z = z_\infty$, and Eq. (40) is marched backwards from $z = z_\infty$ to $z = 0$. Marching the equations in this way ensures that both the boundary conditions on the cylinder surface and the boundary conditions in the far field are utilized.

We now list the marching scheme for (39) with the understanding that a similar scheme, used backwards, is used to integrate (40). The scheme's derivation details can be found in Dennis and Chang [18]. The scheme reads

$$\mathcal{F}_{j+2} = \mathrm{e}^{-2\kappa\Delta z}\mathcal{F}_j + \frac{1}{\kappa}\left(\mathrm{e}^{-2\kappa\Delta z}c_j - c_{j+2}\right) + \frac{1}{2\kappa^2\Delta z}\left[3c_{j+2} - 4c_{j+1} + c_j - \mathrm{e}^{-2\kappa\Delta z}\left(4c_{j+1} - 3c_j - c_{j+2}\right)\right] + \frac{1}{\kappa^3\Delta z^2}\left[2c_{j+1} - c_j - c_{j+2}\right]\left(1 - \mathrm{e}^{-2\kappa\Delta z}\right), \tag{43}$$

which is initiated with the scheme

$$\mathcal{F}_1 = \mathrm{e}^{-\kappa\Delta z}\mathcal{F}_0 + \frac{1}{\kappa}\left(\mathrm{e}^{-\kappa\Delta z}c_0 - c_1\right) + \frac{1}{2\kappa^2\Delta z}\left[c_2 - c_0 - \mathrm{e}^{-\kappa\Delta z}\left(4c_1 - 3c_0 - c_2\right)\right] + \frac{1}{\kappa^3\Delta z^2}\left[2c_1 - c_0 - c_2\right]\left(1 - \mathrm{e}^{-\kappa\Delta z}\right) \tag{44}$$

where $\mathcal{F}_0$ depends on the surface condition.

Lastly, we describe the marching procedure for the case $\kappa = 0$ (hence $n = 0$). Equation (33) becomes

$$\frac{d^2\mathcal{F}}{dz^2} = c(z). \tag{45}$$

Here, $\mathcal{F} = F_0$ since $n = 0$. The problem then amounts to twice numerically integrating the function $c(z)$ using Simpson's rule. We first use the scheme to compute $\mathcal{F}' = \frac{d\mathcal{F}}{dz}$ as follows:

$$\mathcal{F}'_j = \mathcal{F}'_{j-2} + \frac{\Delta z}{3}\left(c_{j-2} + 4c_{j-1} + c_j\right), \tag{46}$$

which is initiated with

$$\mathcal{F}'_1 = \mathcal{F}'_0 + \frac{\Delta z}{24}\left[9c_0 + 19c_1 - 5c_2 + c_3\right]. \tag{47}$$

Once $\mathcal{F}'$ is known, the same marching algorithm, subject to the impermeability condition $\mathcal{F}_0 = 0$, is used again to compute $\mathcal{F}$.

The entire cycle described above is repeated until convergence is reached. The convergence criterion adopted is given by

$$|G_0^{(k+1)}(z, t+\Delta t) - G_0^{(k)}(z, t+\Delta t)| < \varepsilon,\ |G_n^{(k+1)}(z, t+\Delta t) - G_n^{(k)}(z, t+\Delta t)| < \varepsilon,$$
$$\text{and } |g_n^{(k+1)}(z, t+\Delta t) - g_n^{(k)}(z, t+\Delta t)| < \varepsilon \text{ for } n = 1, 2, \ldots, N.$$

Here, the superscripts $k, k+1$ refer to two successive iterates in the cyclic procedure, and ε is some specified tolerance. To initiate the integration procedure, we use the solution at $t = 0$ given by Ψ_{00} and ω_{00} which when expressed in terms of the Fourier coefficients becomes

$$G_0(z, 0) = G_n(z, 0) = g_n(z, 0) = 0,$$
$$F_0(z, 0) = F_n(z, 0) = 0,\ f_1(z, 0) = 2z,\ f_n(z, 0) = 0 \text{ for } n \neq 1,$$

where $n = 1, 2, \ldots, N$.

Presented in the next section are analytical and numerical results along with various comparisons.

5 Results and comparisons

The flow is completely characterized by the Reynolds number, R, and the slip length, β. To confirm numerical convergence, numerous numerical experiments were carried out with different grids and time steps. From these experiments together with the information gained from our analytical solution, we have found the scheme to be both flexible and robust; it requires no relaxation, can run with fairly large time steps, and can even allow the number of terms in the Fourier series to vary during the course of the simulation. The analytical solution reveals that few terms in the series are needed initially, but as time marches on more and more terms are necessary. From our numerical experiments, the following typical values for the computational parameters were used: $z_\infty = 8$, $N = 25$, $\Delta z = 0.05$, and $\varepsilon = 10^{-6}$. We have decided to run the scheme in fully implicit

Table 1 Comparison in C_D between unsteady present and existing steady-state no-slip results for Reynolds numbers $R = 20, 40, 100$

R	References	C_D
20	Present (unsteady, $t = 25$)	2.128
	Dennis and Chang [19] (steady)	2.045
	Fornberg [20] (steady)	2.000
	D'Alessio and Dennis [21] (steady)	1.941
40	Present (unsteady, $t = 25$)	1.612
	Dennis and Chang [19] (steady)	1.522
	Fornberg [20] (steady)	1.498
	D'Alessio and Dennis [21] (steady)	1.443
100	Present (unsteady, $t = 25$)	1.195
	Dennis and Chang [19] (steady)	1.056
	Fornberg [20] (steady)	1.058
	D'Alessio and Dennis [21] (steady)	1.077

mode ($\varpi = 1$). Running in Crank–Nicolson mode ($\varpi = 1/2$) exhibited similar convergence characteristics; however, it produced oscillations in the drag and lift coefficients for a brief time after start up, which is a signature of the Crank–Nicolson scheme. Initial time steps of 10^{-4} were used for the first 10 advances. Then, the next 10 time steps were proceeded with $\Delta t = 10^{-3}$ and continued after with $\Delta t = 0.01$. At $t = 1$, the time step was increased to $\Delta t = 0.05$. No stability difficulties were encountered with the choice of grid and parameters listed above.

Of particular importance is the determination of the drag and lift coefficients, C_D and C_L, respectively, and their variation with time. The dimensionless drag and lift coefficients, obtained by integrating the pressure and frictional stresses on the surface, were computed using the formulae

$$C_D = \frac{2}{R}\int_0^{2\pi}\left(\frac{\partial\zeta}{\partial\xi} - \zeta\right)_0 \sin\theta \mathrm{d}\theta + \frac{\beta^2}{2(1+\beta)^2}\int_0^{2\pi}\zeta_0^2\cos\theta \mathrm{d}\theta - \int_0^{2\pi}\left(\frac{\partial v}{\partial t}\right)_0 \sin\theta \mathrm{d}\theta,$$

$$C_L = \frac{2}{R}\int_0^{2\pi}\left(\zeta - \frac{\partial\zeta}{\partial\xi}\right)_0 \cos\theta d\theta + \frac{\beta^2}{2(1+\beta)^2}\int_0^{2\pi}\zeta_0^2\sin\theta d\theta + \int_0^{2\pi}\left(\frac{\partial v}{\partial t}\right)_0 \cos\theta \mathrm{d}\theta.$$

Derivations of these formulae are outlined in Part 2. We note that for the no-slip case only the first term in these expressions survives, and since we are dealing with symmetric flow $C_L = 0$. The numerical scheme was first tested by setting $\beta = 0$ (i.e., no-slip) and comparing C_D with those reported in previous studies [19–21]. As a check C_L was computed and found to be zero to within our tolerance ε. Shown in Table 1 are comparisons in the drag coefficient for small Reynolds numbers with documented steady-state results. Since our simulation is unsteady, time-stepping was carried out to $t = 25$, when the flow had settled down appreciably. With the passage of time C_D is expected to decrease slowly beyond $t = 25$, and this explains why the present values are slightly larger than the steady-state results.

Next we compare the computed surface vorticity distribution against that predicted by the approximate analytical solution. Using the analytical solution derived in Sect. 3 for the vorticity, the following expression for the surface vorticity $\zeta(0, \theta, t)$ can be obtained:

$$\zeta(0,\theta,t) \sim \frac{2(1+\beta)}{\beta}\left(1 - \frac{\lambda(1+\beta)}{\sqrt{\pi}\beta}\right)\sin\theta.$$

Contrasted in Fig. 2 are surface vorticity distributions at times $t = 0.1, 0.5, 1$ for the case $R = 1000$ and $\beta = 0.5$. These plots serve to illustrate how the agreement between the numerical and analytical solutions is excellent for small times and worsens as time progresses. We see that the agreement is still reasonable at $t = 1$, and at $t = 0.1$ the two solutions are indistinguishable. The general trend observed is that the agreement improves as both R and β increase. As suggested by the analytical solution, the surface vorticity distribution is sinusoidal for small times.

It is well established that for large Reynolds numbers the pressure contribution to C_D, C_L dominates over the frictional component. An important measure of the pressure force is obtained from the dimensionless pressure coefficient (derived in Part 2) given by

$$P^*(\xi = 0, \theta, t) = P(0,\theta,t) - P(0,0,t) = \frac{2}{R}\int_0^{\theta}\left(\frac{\partial\zeta}{\partial\xi}\right)_0 d\bar{\theta} - \frac{\beta^2}{2(1+\beta)^2}\zeta_0^2\Big|_0^{\theta} - \int_0^{\theta}\left(\frac{\partial v}{\partial t}\right)_0 d\bar{\theta}.$$

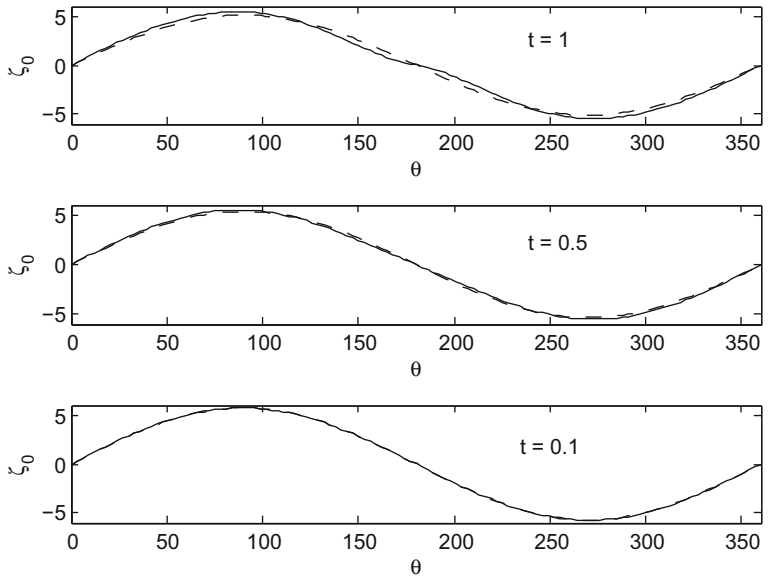

Fig. 2 Numerical (solid line) and analytical (dashed line) surface vorticity distributions for $R = 1000$ and $\beta = 0.5$ at various times

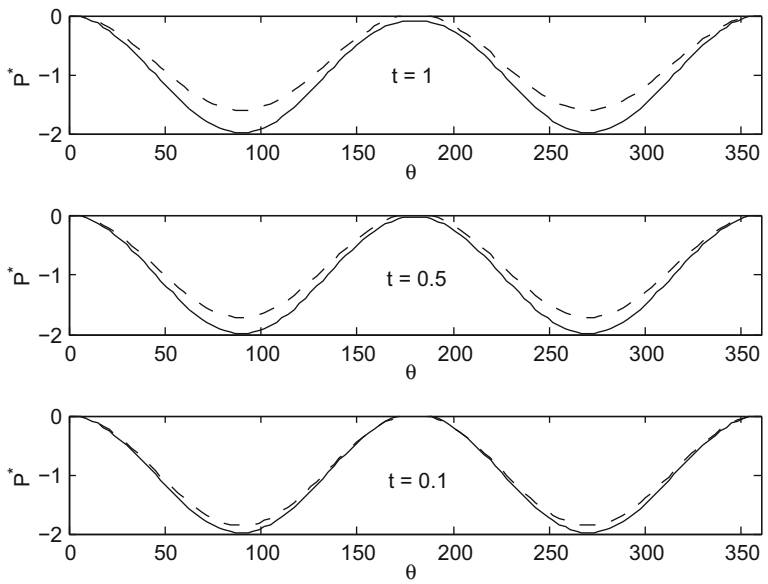

Fig. 3 Numerical (solid line) and analytical (dashed line) pressure coefficient distributions for $R = 1000$ and $\beta = 1$ at various times

The corresponding expression for the inviscid case is easily shown to be

$$P^*(0, \theta) = \cos(2\theta) - 1.$$

Our approximate analytical solution yields the following expression for P^*:

$$P^*(0, \theta, t) \sim \frac{2(1+\beta)(2+\beta)}{\beta^2 R}(1 - \cos\theta) - 2\left(1 - \frac{\lambda(1+\beta)}{\sqrt{\pi}\beta}\right)^2 \sin^2\theta.$$

Displayed in Fig. 3 are comparisons between the numerical and analytical expressions for the case $R = 1000$, $\beta = 1$ at times $t = 0.1, 0.5, 1$. Although the inviscid solution is not drawn, it is clear that there is a good agreement between the numerical, analytical, and inviscid solutions. We emphasize that as t increases

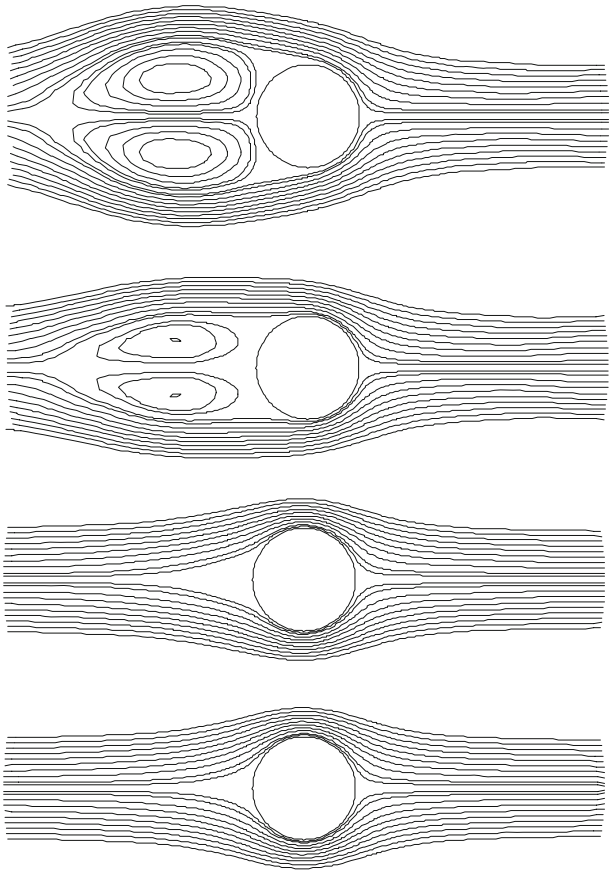

Fig. 4 Streamline plots at $t = 15$ for $R = 500$ and $\beta = 0, 0.1, 0.5, 1$ from top to bottom, respectively

the departure between the viscous and inviscid solutions will become very significant due to boundary-layer separation.

We next present results and streamline flow patterns for $R = 500$. While the numerical scheme described earlier is well suited to capture the early-to-moderate stages of the flow field, for much larger times it will be more appropriate to switch back to the original coordinates (ξ, θ) and solve the system given by (1)–(2) instead of (10)–(11). In this investigation, we have decided to focus on the flow development for early-to-moderate times, $0 < t \leq 15$. For this time interval, we can work entirely in terms of the boundary-layer coordinates (z, θ). We begin by presenting streamline plots of the flow for $R = 500$ at $t = 15$ for various values of β as shown in Fig. 4. It is evident from the plots that as β increases the flow becomes more and more streamlined. This behavior is to be expected. We notice that the wake region behind the cylinder diminishes dramatically with increasing β. In fact, for $\beta = 1$ we observe an almost symmetric flow about the y axis (in addition to the symmetry about the x axis). As the flow becomes more streamlined, we anticipate a reduction in the drag coefficient; this is precisely what we see in Fig. 5 which illustrates the time variation of C_D. For convenience, we have plotted the absolute value of C_D (since C_D will be negative due to the direction of the oncoming flow) and suppressed the rapid reduction in $|C_D|$ from $0 < t < 0.1$ (due to the impulsive start). From this plot, we also notice that for $\beta \neq 0$ the drag coefficient appears to approach a steady-state value. Displayed in Fig. 6 is the distribution of the surface pressure coefficient, P^*, which reveals that as β increases the pressure difference between the front and rear stagnation points decreases. Since the pressure force forms the largest component of the drag, this explains the reduction in drag. Lastly, we present the surface vorticity distribution in Fig. 7 which shows that the distribution becomes more sinusoidal as β increases.

Figure 8 contrasts the development of the flow with time for $R = 1000$ with $\beta = 0$ and $\beta = 1$. The instantaneous flow patterns indicate that a pair of counter-rotating vortices formed between $t = 1$ and $t = 2$ for the no-slip case. With time these vortices grow to create a large wake region behind the cylinder. On the other hand, for the Navier-slip case there is no sign of vortex formation nor is there any evidence of shed

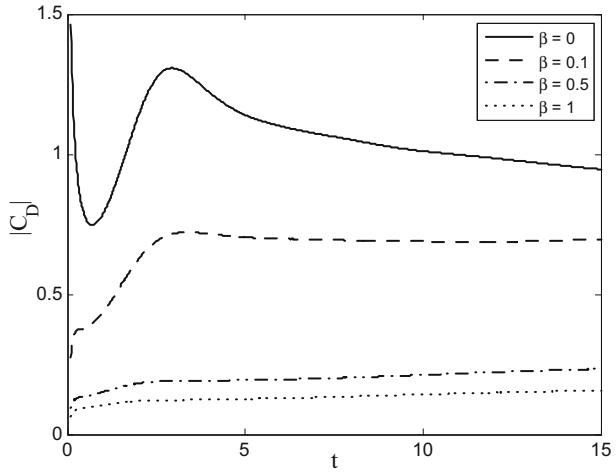

Fig. 5 Time variation of C_D for $R = 500$ and $\beta = 0, 0.1, 0.5, 1$

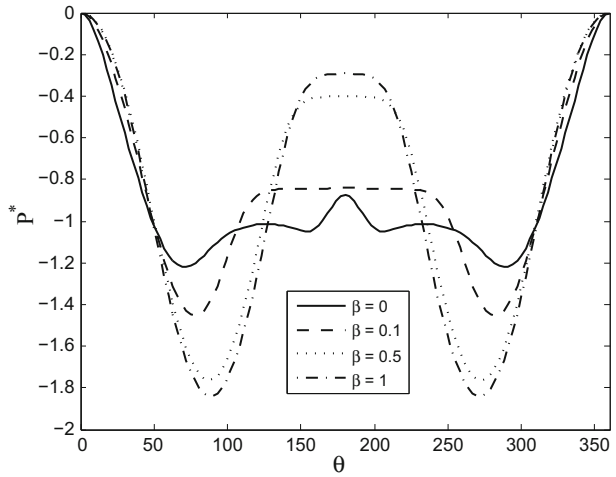

Fig. 6 The distribution of P^* at $t = 15$ for $R = 500$ and $\beta = 0, 0.1, 0.5, 1$

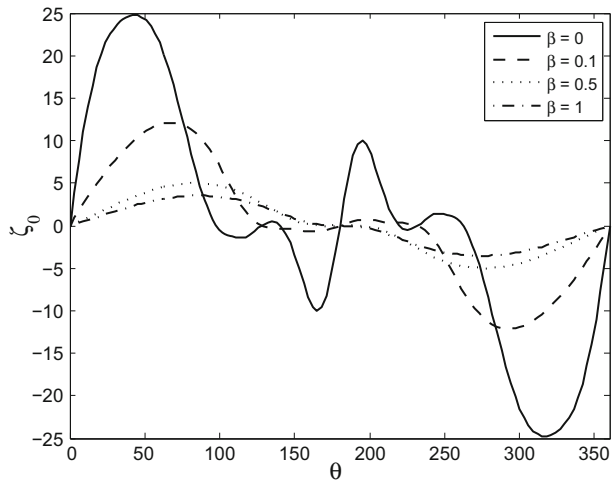

Fig. 7 The surface vorticity distribution at $t = 15$ for $R = 500$ and $\beta = 0, 0.1, 0.5, 1$

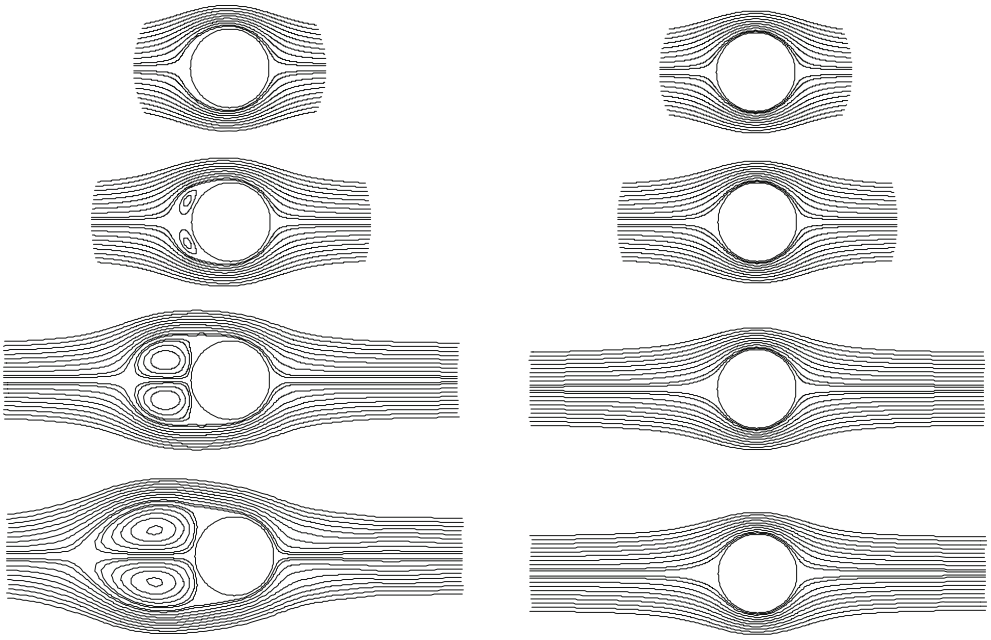

Fig. 8 Streamline plots for $R = 1000$ at $t = 1, 2, 5, 10$ from top to bottom, respectively, with $\beta = 0$ (left) and $\beta = 1$ (right)

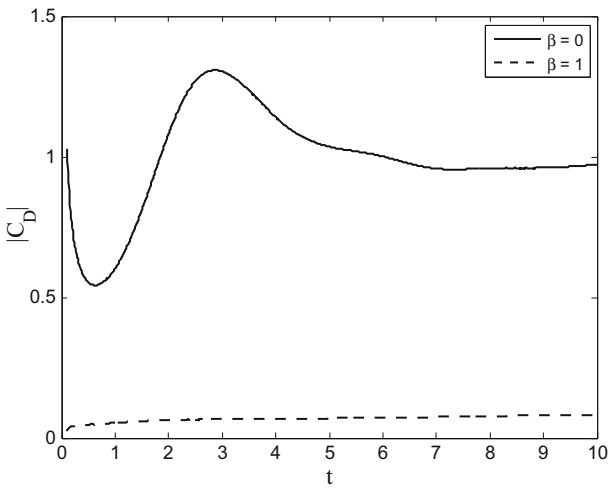

Fig. 9 Time variation of C_D for $R = 1000$ and $\beta = 0, 1$

vortices. The associated time variation of the drag coefficient and distributions of the surface pressure and vorticity is displayed in Figs. 9, 10, 11, respectively. These plots are very similar to the corresponding plots previously presented for the case $R = 500$.

We lastly comment on the suppression of flow separation. As indicated in Fig. 4, the slip condition seems to suppress the tendency for flow separation as β increases. This was investigated further by estimating the critical value of β, denoted by β_c, where flow separation is suppressed. Numerous numerical simulations were performed to estimate β_c over the time intervals considered for $R = 100$, 500, and 1000. The value of β_c was determined by applying the vanishing surface vorticity condition as follows. For a given Reynolds number with $\beta = 0$, the separation angle, θ_s, was found by estimating where the surface vorticity changes sign. As β increased θ_s also increased, and by incrementing β we were able to estimate when $\theta_s = 180°$ which we defined as β_c. We discovered that for $R = 100$ the value of β_c occurred in the interval $0.6 < \beta_c < 0.65$. This was repeated for $R = 500$ and $R = 1000$, and β_c was found to lie in the interval $0.7 < \beta_c < 0.75$ for both cases. Thus, there appears to be little variation in β_c with the Reynolds number over the range $100 \leq R \leq 1000$.

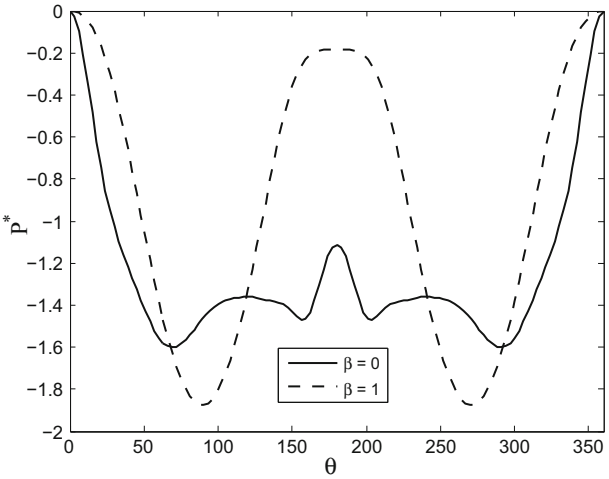

Fig. 10 The distribution of P^* at $t = 10$ for $R = 1000$ and $\beta = 0, 1$

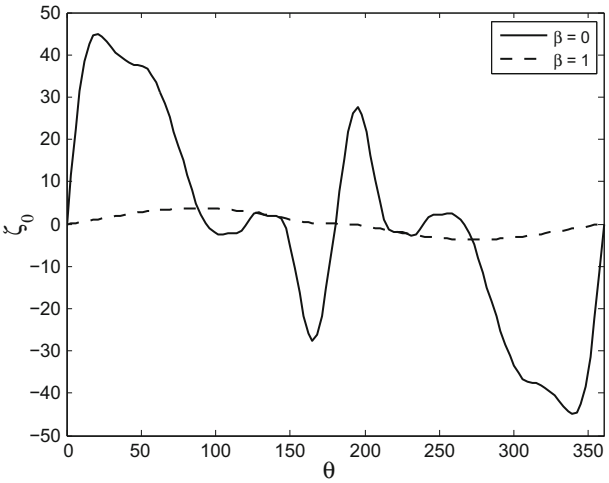

Fig. 11 The surface vorticity distribution at $t = 10$ for $R = 1000$ and $\beta = 0, 1$

6 Conclusions

Considered in this paper is the unsteady two-dimensional laminar flow of a viscous incompressible fluid past a circular cylinder subject to impermeability and Navier-slip surface conditions. To adequately model the evolving early flow development and to sufficiently resolve the thin boundary layer, a transformation was introduced. This boundary-layer type transformation incorporated the known early structure of the flow into the equations of motion. A numerical technique involving both finite difference and spectral methods was described and successfully implemented to compute the early-to-moderate stages of the flow following the start of the motion for moderate-to-large Reynolds numbers. Also presented was an approximate series solution expressed in powers of the time t and the parameter $\lambda = \sqrt{8t/R}$. Excellent agreement was found between the approximate and numerical solutions for small times and moderately large Reynolds numbers. Comparisons with documented results for the no-slip case also revealed good agreement.

Various results including streamline plots, surface vorticity and pressure coefficient distributions, and time variations in the drag coefficient were presented for Reynolds numbers 500 and 1000 and for small-to-moderate times. The key finding is that a reduction in the drag coefficient results from the Navier-slip condition when compared to the no-slip condition. This reduction increases as the slip length increases. Our results are consistent with those made by previous investigations. The streamline plots for the no-slip case can be characterized as having a large wake region containing a pair of counter-rotating vortices, while for the Navier-slip case the streamline plots can be profoundly different depending on the value of β. For example,

when $\beta = 1$ there is no apparent wake region forming behind the cylinder for small-to-moderate times for $R = 500$ and $R = 1000$. That is, flow separation is suppressed. The critical value of β leading to the suppression of flow separation was estimated for various Reynolds numbers and was found to remain fairly constant in the range $100 \leq R \leq 1000$. Also, the pressure difference between the front and rear stagnation points decreases as β increases with $\beta = 0$ possessing the largest difference. Although the flow considered in Part 1 was symmetric, Part 2 of this investigation will focus on asymmetric flow past an inclined elliptic cylinder.

Acknowledgements Financial support for this research was provided by the Faculty of Mathematics at the University of Waterloo.

References

1. Zdravkovich, M.M.: Flow Around Circular Cylinders. Vol. 1: Fundamentals. Oxford University Press, Oxford (1997)
2. Zdravkovich, M.M.: Flow Around Circular Cylinders, Vol. 2: Applications. Oxford University Press, Oxford (2003)
3. Navier, C.L.M.H.: Memoire sur les lois du mouvement des fluides. Mem. Acad. R. Sci. Inst. France **6**, 389–440 (1823)
4. Rothstein, J.P.: Slip on superhydrophobic surfaces. Ann. Rev. Fluid Mech. **42**, 89–109 (2010)
5. Ajaev, V.S.: Interfacial Fluid Mechanics: A Mathematical Modeling Approach. Springer, New York (2012)
6. Beavers, G.S., Joseph, D.D.: Boundary conditions at a naturally permeable wall. J. Fluid Mech. **30**, 197–207 (1967)
7. Saffman, P.: On the boundary condition at the interface of a porous medium. Stud. Appl. Maths **1**, 93–101 (1971)
8. You, D., Moin, P.: Effects of hydrophobic surfaces on the drag and lift of a circular cylinder. Phys. Fluids **19**, 081701 (2007)
9. Seo, I.W., Song, C.G.: Numerical simulation of laminar flow past a circular cylinder with slip conditions. Int. J. Numer. Methods Fluids **68**, 1538–1560 (2012)
10. Li, D., Li, S., Xue, Y., Yang, Y., Su, W., Xia, Z., Shi, Y., Lin, H., Duan, H.: The effect of slip distribution on flow past a circular cylinder. J. Fluids Struct. **51**, 211–224 (2014)
11. Williamson, C.H.K.: The existence of two stages in the transition to three-dimensionality of a circular wake. Phys. Fluids **31**, 3165–3168 (1988)
12. Blackburn, H.M., Henderson, R.D.: A study of two-dimensional flow past an oscillating cylinder. J. Fluid Mech. **385**, 255–286 (1999)
13. Nield, D.A., Bejan, A.: Convection in Porous Media, 3rd edn. Springer, Berlin (2006)
14. Dennis, S.C.R., Quartapelle, L.: Some uses of Green's theorem in solving the Navier–Stokes equations. Int. J. Numer. Methods Fluids **9**, 871–890 (1989)
15. Badr, H.M., Dennis, S.C.R.: Time-dependent viscous flow past an impulsively started rotating and translating circular cylinder. J. Fluid Mech. **158**, 447–488 (1985)
16. Collins, W.M., Dennis, S.C.R.: Flow past an impulsively started circular cylinder. J. Fluid Mech. **60**, 105–127 (1973)
17. Rohlf, K., D'Alessio, S.J.D.: Uniform shear flow past a circular cylinder. Acta Mech. **178**, 199–222 (2005)
18. Dennis, S.C.R., Chang, Gau-Zu: Numerical integration of the Navier–Stokes equations in two dimensions, Mathematics Research Center, University of Wisconsin. Technical Summary Report No. 859 89pp (1969)
19. Dennis, S.C.R., Chang, G.-Z.: Numerical solutions for steady flow past a circular cylinder at Reynolds numbers up to 100. J. Fluid Mech. **42**, 471–489 (1970)
20. Fornberg, B.: A numerical study of steady viscous flow past a circular cylinder. J. Fluid Mech. **98**, 819–855 (1980)
21. D'Alessio, S.J.D., Dennis, S.C.R.: A vorticity model for viscous flow past a cylinder. Comp. Fluids **23**, 279–293 (1994)